Effect of tow thickness on the structural response of aerospace-grade spread-tow fabrics

Arteiro, A., Catalanotti, G., Xavier, J., Linde, P., & Camanho, P. P. (2017). Effect of tow thickness on the structural response of aerospace-grade spread-tow fabrics. *Composite Structures*, *179*, 208-223. https://doi.org/10.1016/j.compstruct.2017.06.047

Published in:
Composite Structures

Document Version:
Peer reviewed version

Effect of tow thickness on the structural response of aerospace-grade spread-tow fabrics

A. Arteiro[a,*], G. Catalanotti[b], J. Xavier[c,d], P. Linde[e], P.P. Camanho[a,c]

[a] *DEMec, Faculdade de Engenharia, Universidade do Porto, Rua Dr. Roberto Frias, s/n, 4200-465 Porto, Portugal*
[b] *School of Mechanical and Aerospace Engineering, Queen's University Belfast, Belfast, BT9 5AH, UK*
[c] *INEGI, Instituto de Ciência e Inovação em Engenharia Mecânica e Engenharia Industrial, Rua Dr. Roberto Frias, 400, 4200-465 Porto, Portugal*
[d] *CITAB, Universidade de Trás-os-Montes e Alto Douro, Engenharias I, Apartado 1013, 5001-801 Vila Real, Portugal*
[e] *AIRBUS Operations GmbH, Kreetslag 10, 21129 Hamburg, Germany*

Abstract

The effect of ply thickness on the onset of intralaminar and interlaminar damage is extremely important for the structural response of laminated composite structures. This subject has gained particular interest in recent years due to the introduction in the market of spread-tow, ultra-thin carbon-fibre reinforcements with different configurations. In the present paper, an experimental test campaign was carried out to study the structural response of aerospace-grade plain weave spread-tow fabrics (STFs) of different areal weights. The results showed that, in spite of an apparent superior longitudinal tensile strength of the thick STF, the multidirectional thin-STF laminate exhibited an improved tensile unnotched strength over the thick-STF laminate, attributed to its damage suppression capability. However, damage suppression was also responsible for similar tensile notched strengths. In compression, the thin-STF laminate performed substantially better than the thick-STF laminate in both unnotched and notched configurations. Finally, a similar bearing response was obtained in both STF laminates, in spite of a slightly higher resistance of the thin-STF laminate to the propagation of subcritical damage mechanisms.

*Corresponding author. Tel.: +351 220414049.
Email address: aarteiro@fe.up.pt (A. Arteiro)

Keywords: Polymer-matrix composites (PMCs), Spread-tow fabrics, Mechanical properties, Mechanical testing

1. Introduction

The thinner and wider tows obtained with tow spreading show unique benefits that open a broad range of new possibilities in terms of design and manufacturing of composite structures. For example, spread-tow fabrics (STFs) can be obtained using spread tapes in the weaving process instead of conventional yarns. Using spread tapes, fibre bundles are not only thinner, but they are also wider, resulting in flatter fabrics, with fewer interlacing points and better surface finish than conventional ones. Such fabric configurations are also characterised by minimal fibre waviness, and therefore lower crimp frequency and smaller crimp angles [1, 2], allowing the filaments to immediately carry tensile or compressive loads without first having to straighten.

Due to the thinner and wider spread tows, the amount of matrix between the tows of thin-ply fabrics is also very small, resulting in overall composite fibre volume fractions very close to the local fibre volume fraction of the spread tows [3, 4]. As a result, the performance of thin-ply fabrics can approach that of laminates made of unidirectional (UD) tapes.

In the present work, the effect of tow thickness on the structural response of aerospace-grade spread-tow fabrics was investigated. An experimental test campaign was carried out to study the structural response of aerospace-grade plain weave STFs with different areal weights. The test campaign included characterisation tests of the STFs, performed on simple UD STF laminates, and the detailed assessment of the structural response of multidirectional STF laminates defined based on a baseline of the aeronautical industry.

2. Material selection and manufacturing

T700SC TeXtreme® STFs from Oxeon AB pre-impregnated with HexPly® M21 toughened epoxy resin from Hexcel (with a nominal 35% resin content)

were selected for this study. Two plain weave configurations with different areal weights were used: 160 g/m^2 and 240 g/m^2 STFs, with nominal fabric layer thicknesses around 0.16 mm and 0.24 mm respectively.

The characterisation of the 160 g/m^2 and 240 g/m^2 STFs was performed on UD textile laminates with a plain weave (cross-ply) configuration. Two multidirectional textile laminates, one of each STF grade, were also designed based on a damage tolerance optimised baseline laminate for aeronautical applications.

Table 1 shows the stacking sequences definition. The 0° orientation is coincident with the loading direction. All selected laminates are balanced and symmetric (due to the plain weave configuration). The multidirectional structural laminates are orthotropic. These laminates were designed to match as possible the thickness and stiffness of the baseline multidirectional laminate. However, due to constraints in the stacking sequence imposed by the different thickness of the *prepreg* weaves, laminates with different elastic properties (expectably in the range of 3% for the Young's moduli, 4% for the shear modulus, and 5% for the Poisson's ratio) and different thickness (Table 1) had to be considered.

All laminates were prepared for curing in a vacuum bag and cured using an autoclave. The autoclave cure cycle was defined by setting a heat-up rate of 2°C/min from room temperature to 180°C, holding at 180°C for 120 minutes and cooling down at a rate of 2°C/min. A gauge autoclave pressure of 4 bar was applied throughout the cure cycle. After curing, each plate was cut to the nominal dimensions of the specimens using a diamond-coated disk.

3. Experimental test programme

3.1. Strength characterisation tests

Unnotched tension and compression tests were performed on UD specimens, including off-axis compression tests. All tests were performed under displacement control. The tension tests were conducted at a speed of 1.0 mm/min in an MTS 810 servo-hydraulic testing machine with a load capacity of 250 kN, equipped with a 250 kN load cell. The specimens were fixed to the load frame

using a bolted clamping rig, and sandpaper was inserted between the specimen surfaces and the grips to improve the load transfer capability and prevent sliding. The compression tests were performed in an Instron 4208 electro-mechanical universal testing machine (load capacity of 300 kN) equipped with a 100 kN load cell at a controlled speed of 0.1 mm/min.

3.1.1. Fabric tensile unnotched strength

Plain weave unnotched specimens with a nominal width (W) of 25 mm and a nominal length (L_s) of 300 mm were tested in tension, following the ASTM D3039/D3039M – 14 test standard [5]. The tests were performed on laminates *UDA240* and *UDA160* (Table 1). The gauge length (L) of the specimens was set to 150 mm.

3.1.2. Fabric compressive unnotched strength

Unnotched compression tests were performed on laminates *UDB240* and *UDB160* (Table 1). Following Koerber et al. [6], specimens with a nominal width (W) of 10 mm and a nominal length (L) of 20 mm were tested using an end-loading test rig with a self-alignment system. Polished tungsten-carbide (TC) inserts were used to avoid damage on the contact surfaces of the test fixture caused by the endings of the stiff carbon fibres [6, 7]. In addition, a thin layer of molybdenum disulphide (MoS_2) was used between the specimen end-surfaces and the surfaces of the rig to minimise friction [6].

3.1.3. Fabric off-axis compression tests

Off-axis specimens provide a simple way of studying the mechanical behaviour of UD composites and laminates under combined stresses, useful to derive experimental yield and failure envelopes. In the present work, 15° and 30° off-axis compression tests were performed. These tests were carried out on laminates *UDB240* and *UDB160*.

Following Koerber et al. [6], unnotched specimens with a nominal width (W) of 10 mm and a nominal length (L) of 20 mm were tested using the same end-loading test rig used in the UD unnotched compression tests (Sect. 3.1.2). To

determine the strength components of the off-axis tests, $\bar{\sigma}_{11}$, $\bar{\sigma}_{22}$ and $\bar{\sigma}_{12}$, the measured axial compressive strength in the loading coordinate system, $\bar{\sigma}_x$, needs to be transformed into the material coordinate system. This can be performed employing a simple coordinate transformation [6]:

$$\bar{\sigma}_{11} = \bar{\sigma}_x \cos^2 \theta \tag{1}$$

$$\bar{\sigma}_{22} = \bar{\sigma}_x \sin^2 \theta \tag{2}$$

$$\bar{\sigma}_{12} = -\bar{\sigma}_x \sin \theta \cos \theta \tag{3}$$

where the transformation angle $\theta = \theta_0 + \Delta\theta$ consists of the initial off-axis angle, θ_0, and the additional fibre rotation, $\Delta\theta$, occurring due to the extension-shear coupling effect [6]. The additional fibre rotation $\Delta\theta$ can be measured via post-processing of full-field measurements obtained using, for example, the digital image correlation (DIC) technique (Sect. 4). It is important to note that the strength components of the off-axis tests, $\bar{\sigma}_{11}$, $\bar{\sigma}_{22}$ and $\bar{\sigma}_{12}$, expressed in the material coordinate system, are not the ply strengths for uniaxial loading along the main material directions.

According to Koerber et al. [6], the off-axis specimens with the proposed geometry are characterised by a large barreling deformation at high axial compressive strains. To avoid overpredicting the actual axial compressive strength, the true specimen cross section should be used in the calculation of the applied axial stress. Following Koerber et al. [6], the true specimen cross section can be estimated applying a volume consistency condition:

$$S = S_0 \frac{L_0}{L} = S_0 \left(1 - \frac{\Delta L}{L_0}\right)^{-1} \tag{4}$$

where $S_0 = W \times t$ is the initial cross-section area, L_0 and L are respectively the initial and current specimen length, and ΔL is the specimen length change given by the relative displacement, in the loading direction, between two points near the top and bottom loading surfaces. This relative displacement can be obtained, for example, from the in-plane displacement field measured using the

DIC technique (Sect. 4).

3.2. Structural tests

To assess the effect of the grade of the STFs on the mechanical response of structural laminates, tension, compression and bearing tests were performed on the multidirectional STF laminates *DTO240* and *DTO160* (Table 1). The tension tests were performed in an MTS 810 servo-hydraulic testing machine with a load capacity of 250 kN, equipped with a 250 kN load cell. The compression and bearing tests were performed in an MTS 810 testing machine with a load capacity of 100 kN, equipped with a 100 kN load cell. All tests were performed at a controlled speed of 1.0 mm/min.

Following the ASTM D6484/D6484M – 14 test standard [8], a special test rig designed to prevent buckling was used in the compression tests. The alignment of the clamping system with the axis of the testing machine was performed using two guiding pins with a diameter of 6 mm in the ends of the specimens.

The guiding holes in the compression specimens [8] and the open holes and notches machined to assess the notched response of laminates *DTO240* and *DTO160* were obtained using a drilling or a milling machine, respectively. Carbon-epoxy sacrificial plates were used at the insertion and exit points of the drill bit to avoid damage during the machining process. A 1 mm drill bit was used to machine the sharp notches, ensuring a distance of 1 mm between the notch faces. A constant width-to-notch length ratio ($W/2a$) equal to 6 was considered.

3.2.1. Laminate tensile and compressive unnotched strengths

In this work, unnotched specimens with a nominal width (W) of 25 mm and a nominal length (L_s) of 300 mm were tested in tension following the ASTM D3039/D3039M – 14 test standard [5]. The gauge length (L) was set to 150 mm. Unnotched compression tests were conducted on specimens with a nominal width of 25 mm and a nominal length of 305 mm.

3.2.2. Laminate tensile centre-notched strength

To understand the mechanical performance and structural integrity of the STF laminates in the presence of high stress concentrations, Centre-Notched Tension (CNT) tests were carried out in the present work. CNT specimens with a nominal width (W) of 30 mm and a nominal length (L_s) of 300 mm were tested. The gauge length (L) was set to 150 mm. A centre notch with a nominal length ($2a$) of 5 mm was used.

3.2.3. Laminate compressive centre-notched strength

In the present work, Centre-Notched Compression (CNC) tests were conducted on specimens with a nominal width (W) of 30 mm and a nominal length (L_s) of 305 mm. The centre notch had a nominal length ($2a$) of 5 mm. The separation of 1 mm between the crack faces was sufficient to avoid contact between the crack faces after compressive failure.

3.2.4. Open-Hole Tension (OHT) tests

In the present work, Open-Hole Tension (OHT) tests were carried out to evaluate the mechanical behaviour in the presence of stress concentrations, based on the ASTM D5766/D5766M – 11 test standard [9]. OHT specimens of different sizes were tested. Table 2 shows the OHT test matrix, where W is the nominal specimen width, L_s is the nominal specimen length, L is the gauge length (free length between grips), and d is the hole diameter. The width-to-hole diameter ratio (W/d) was constant and equal to 6.

3.2.5. Open-Hole Compression (OHC) tests

Open-Hole Compression (OHC) tests were conducted on specimens with a nominal width (W) of 30 mm and a nominal length (L_s) of 305 mm. The nominal hole diameter (d) was 5 mm, resulting in a width-to-hole diameter ratio (W/d) equal to 6.

3.2.6. Bearing tests

Mechanically fastened joints are generally the critical part of a composite structure, as they are a source of weakness and compliance. Following the ASTM D5961/D5961M – 13 test standard [10], bolt-bearing tests were performed in the present study. Specimens with a nominal hole diameter (d) of 6 mm, end distance-to-hole diameter ratio $e/d = 6$, width-to-hole diameter ratio $W/d = 6$, and nominal length (L_s) of 215 mm were tested. A bolt M6 was used with a washer subjected to a "finger-tight" clamping pressure, corresponding to a torque $T = 2.2$ Nm. The end of the specimen far from the bearing hole was clamped using a bolted clamping rig. The alignment of the longitudinal axis of the gripped specimen with the test direction was performed using a guiding pin with a diameter of 4 mm.

4. Instrumentation

The experimental monitoring of damage and fracture phenomena in composite materials using optical full-field techniques can be extremely useful to identify and understand the complex failure behaviour of these materials [11–15]. In this experimental programme, full-field measurements were performed using the DIC technique to obtain the surface in-plane displacement and strain fields of the outer (0/90) STF layer. Measurements were performed in at least one representative specimen of each laminate and test configuration. These results were used to assist in the assessment of strain concentrations and to monitor the differences in damage formation and propagation in the different STF laminates.

All measurements were performed by means of a single camera, using the ARAMIS DIC-2D v6.0.2 system developed by GOM [16]. The optical system, its characteristics and the adopted configuration are summarised in Table 3.

5. Experimental results and discussion

5.1. *Strength characterisation test results*

5.1.1. *Fabric tensile unnotched strength test results*

As expected, linear stress-strain relations up to the ultimate remote stress were obtained in both STFs (Fig. 1). Prior to ultimate failure, transverse matrix cracking had not occurred (Fig. 2). Both STFs were characterised by a catastrophic fibre-dominated failure mode, with evidence of transverse and longitudinal split cracking of the spread-tow yarns (Fig. 3). The *UDA240* STF laminate also exhibited gauge section delamination between the STF layers (Fig. 3a), which was reduced in the *UDA160* STF laminate (Fig. 3b). It was also noted that the 240 g/m^2 STF was more susceptible to fibre-matrix splitting than the thinner 160 g/m^2 STF.

Table 4 shows the measured longitudinal Young's moduli E_{1T}, Poisson's ratios ν_{12} and mean tensile unnotched strengths X_T of the 240 g/m^2 and 160 g/m^2 STFs. Interestingly, the difference in the Young's moduli is negligible. However, the tensile strength of the thinner 160 g/m^2 STF is 7.2% lower than the tensile strength of the 240 g/m^2 STF, which is not in line with the results reported in the literature for multidirectional[1] tape laminates [13, 17–19]. Apparently, due to the woven reinforcement architecture, the susceptibility of the 240 g/m^2 STF for earlier development of fibre-matrix splitting leads to some relaxation of the highly stressed longitudinal yarns, which delays the laminate final fracture, an effect not observed in unnotched multidirectional tape laminates.

5.1.2. *Fabric compressive unnotched strength test results*

In the unnotched compression tests, before ultimate failure, modest load drops were observed in both STFs, with a negligible effect on the stiffness of the tested specimens; in some cases, the first load drop was also the peak load.

[1]Even though the results presented in Sect. 5.1.1 refer to UD textile laminates, these include both 0° and 90° tapes in their architecture, making them comparable to cross-ply tape laminates.

These load drops can be attributed to the development of compressive damage, in the form of kink bands or brittle, shear-driven compressive cracks, which could be observed in the failed specimens after testing (Fig. 4).

Final failure was catastrophic in all specimens, characterised by a total loss of load-carrying capacity (sudden load drop, down to practically zero). However, ultimate failure was not due to the propagation of compressive fibre failure through the thickness of the specimen, but it occurred due to layer splitting along the length of the specimen, induced by localised longitudinal compressive failure of thin sublaminates (see Fig. 4).

Table 4 shows the measured longitudinal Young's moduli E_{1C} and mean compressive unnotched strengths X_C of the 240 g/m^2 and 160 g/m^2 STFs. It is interesting to note that the difference in Young's moduli is not only small between *prepreg* weaves, but also between the tensile and compressive loading conditions (Table 4). It should be noted that this is often not the case in woven fabrics (e.g. Ref. [2]). On the other hand, the thinner 160 g/m^2 STF exhibits a compressive unnotched strength 16.2% higher than the 240 g/m^2 STF. This superior compressive unnotched response can be attributed not only to an improved uniformity of the microstructure of spread tows [19], but also to a better uniformity of the woven architecture, including lower fibre waviness and smaller crimp angles, which delay micro- and meso-instabilities in the fibre direction and, consequently, improve the longitudinal compressive strength.

5.1.3. Off-axis compression test results

As suggested by Koerber et al. [6], the axial stress, σ_x, and the axial compressive strength, $\bar{\sigma}_x$, were calculated dividing respectively the load signal and the peak load by the true specimen cross section (Eq. (4)), determined based on the relative displacement obtained from a representative specimen of each off-axis angle and STF grade.

In the 15° off-axis compression tests, a small nonlinearity before ultimate failure was observed. A single kink band penetrating completely through the thickness of the specimen, approximately perpendicular to the off-axis direction,

or a series of kink bands had formed along the length of the 15° off-axis specimens (Fig. 5). Surface crushing was observed on the failed specimens at the loaded ends. Small delaminations from the end surfaces were often observed. Some 15° off-axis specimens also exhibited a "brush"-like layer splitting failure mode, with no clear longitudinal compressive failure mode. Nevertheless, the different failure modes had no effect on the ultimate failure stress of the 15° off-axis compression tests.

The 30° off-axis compression tests exhibited a marked nonlinear response, attributed to high localised plastic deformation and to an accumulation of compressive damage. Ultimate failure generally occurred quickly, with a steep load drop. However, due to the large accumulation of damage, this sudden load drop was not catastrophic, but resulted from extensive material degradation. During damage accumulation, small buckling edge delaminations of thin outer sublaminates were observed (Fig. 6), followed by crushing of one of the corners of the loaded ends. Finally, the load started dropping quickly. This was apparently due to compression stability failure of the fibres or due to severe out-of-plane layer splitting. Some specimens exhibited surface crushing, with a "brush"-like layer splitting failure mode (Fig. 6). Marked kink bands, approximately perpendicular to the off-axis direction, which penetrate partially through the thickness of the specimens, could also be observed (Fig. 6). In some cases, delaminations propagated from the kink bands towards one of the ends of the specimen, which prevented the kink bands from extending completely through the thickness.

Table 5 shows the mean axial compressive strengths, $\bar{\sigma}_x$, of the 240 g/m^2 and 160 g/m^2 STFs for the 15° and 30° off-axis tests, and the respective coefficients of variation. Interestingly, the axial compressive strength of the 15° off-axis specimens of both laminates is virtually the same; it differs by just 1.3%. In fact, no difference was observed between the mechanical response and failure modes of the 15° off-axis specimens of the 240 g/m^2 and 160 g/m^2 STFs. On the other hand, the thinner 160 g/m^2 STF exhibits a 30° off-axis axial compressive strength 16.9% higher than the 240 g/m^2 STF (a difference in the range of that observed for the unnotched compressive strengths in Sect. 5.1.2).

Figure 7 shows the failure envelopes of the 240 g/m^2 and 160 g/m^2 STFs for the combined compression/in-plane shear stress space σ_{11}–σ_{12} (in the material coordinate system), obtained from the measured axial compressive strength in the loading coordinate system, $\bar{\sigma}_x$, using Eqs. (1)–(3). The correct off-axis angle at failure, θ, was obtained from the DIC data of a representative specimen of each off-axis configuration and STF.

Due to the balanced amount of fibres in the warp- and weft-direction, it can be assumed that the corresponding compressive strengths are equal (i.e. $X_C = Y_C$), and the 15° and 30° off-axis data can be used to represent fictitious 75° and 60° off-axis specimens, respectively. By simply interchanging the warp and weft stress components, the data points for fictitious 75° and 60° off-axis specimens can be obtained. These data points are also plotted in the σ_{11}–σ_{12} stress diagram of Fig. 7.

As observed by Koerber et al. [6] for a 5-harness-satin textile carbon-epoxy composite, an approximately constant value of the in-plane shear stress at failure was obtained regardless of the applied multiaxial stress state. A maximum stress failure criterion seems therefore suitable to approximate the failure envelopes of the STFs studied in the present work (Fig. 7). Hence, the obtained off-axis data can be used to estimate the in-plane shear strengths (S_L) of the STFs investigated in the present study (see × data points in Fig. 7). The resulting in-plane shear strengths are respectively $S_L = 71$ MPa and $S_L = 75$ MPa for the 240 g/m^2 and 160 g/m^2 STFs, a difference of 5.6%. The meso-structure of the textile composites, which resembles a cross-ply laminate, apparently promotes a thickness effect on the in-plane shear strength. In fact, Fig. 7 shows that the thinner 160 g/m^2 STF not only exhibits a markedly superior behaviour in compression, attributed to the uniformity of the thinner reinforcement architecture of the 160 g/m^2 STFs (Sect. 5.1.2), but also a slightly higher in-plane shear strength, which can be attributed to the ability of the thinner spread-tow yarns to suppress microcracking caused by shear loading (*in situ* effect [20]). On the other hand, from the 30° off-axis specimens, for example, it is possible to estimate the shear modulus, G_{12}, of the plain weaves from the measured off-

axis stiffness and using Laminated Plate Theory [21]. A small difference, in the range of 5%, was obtained (Table 5). It is interesting to note that, despite the differences in the strengths of the STFs, the differences in the measured elastic properties are practically negligible.

5.2. Structural test results

5.2.1. Laminate tensile unnotched strength test results

Laminate *DTO160* was characterised by an approximately linear remote stress-strain relation up to ultimate failure (Fig. 8). Laminate *DTO240*, on the other hand, exhibited a minor nonlinear behaviour close to the ultimate load (Fig. 8), resulting in a slightly higher failure strain $\bar{\epsilon}_x$ (Table 6). However, laminate *DTO160* exhibits a tensile unnotched strength, X_T^L, 13.9% higher than laminate *DTO240*. This improved laminate unnotched response is attributed to the damage suppression capability of laminates made of thinner reinforcements [13, 17, 19]. On the other hand, the nonlinear response of laminate *DTO240* can be attributed to the development of subcritical damage, including matrix cracking of the transverse spread-tow yarns and longitudinal splitting along the 0° spread-tow yarns (Fig. 9), and to the nonlinear behaviour of the off-axis STFs.

At failure, both laminates exhibited a catastrophic fibre-dominated failure mode (Fig. 10). However, laminate *DTO240* (Fig. 10a) was characterised by extensive pull-out, with transverse and longitudinal split cracking along the transverse and longitudinal spread-tow yarns, respectively. A diffuse failure region was observed, without a clear fracture plane. Laminate *DTO160* (Fig. 10b), as expected, exhibited a more brittle net-section failure mode, with a fracture plane perpendicular to the loading direction. Matrix damage and fibre-matrix splitting was effectively precluded when reducing the yarns grade from 240 g/m^2 to 160 g/m^2, resulting in an improved unnotched response (see Table 6). Gauge section delamination was not observed in the tested multidirectional fabric laminates.

Table 6 also shows the measured Young's modulus, E_x, of both laminates.

As can be observed, laminate *DTO160* is stiffer than laminate *DTO240*, which partially explains the higher strength of the former. Nevertheless, the thickness effect is expected to have the largest contribution for this improved strength.

It is also interesting to note that the apparent superior longitudinal strength of the 240 g/m^2 STF reported in Sect. 5.1.1 did not translate into a superior laminate strength. If, in the former, subcritical damage growth (mostly longitudinal splitting — Fig. 2), apparently resulted in the relaxation of the longitudinal yarns, delaying ultimate failure, in the latter, transverse cracking and longitudinal splitting (Fig. 9) caused local stress redistributions that promoted earlier laminate failure, reducing the laminate unnotched strength, as observed elsewhere [13, 17–19].

5.2.2. Laminate compressive unnotched strength test results

Before compressive failure, small load drops were observed in some specimens of both laminates, with a negligible effect on the stiffness of the tested specimens. These can be attributed to the development of compressive damage before ultimate failure, which was sudden and catastrophic, characterised by a big load drop. After testing, all specimens exhibited a net-section failure mode, characterised by a complex combination of damage mechanisms, including fibre kinking, wedge transverse fracture, delamination and surface fibre/matrix splitting caused by buckling of the outer STF layers (Fig. 11).

Laminate *DTO160* exhibited a slightly more brittle failure mode, with a more clear through-the-thickness fracture plane, inclined with respect to the mid-plane of the specimen (Fig. 11b). Delamination between STF layers was absent. In laminate *DTO240*, on the other hand, a more diffuse fracture region was observed, including free-edge delamination along the outer STF layers (Fig. 11a).

Table 6 shows the mean laminate compressive unnotched strengths, X_C^L, of laminates *DTO240* and *DTO160*. Laminate *DTO160* exhibits a compressive unnotched strength 17.7% higher than laminate *DTO240*, which can be attributed to the uniformity of the thinner reinforcement architecture of the

160 g/m^2 STFs of laminate *DTO160*. In fact, the thinner 160 g/m^2 STF exhibits higher compressive strength than the 240 g/m^2 STF (Sect. 5.1.2), as the better uniformity of the spread-tow yarns, lower fibre waviness and smaller crimp angles of the former can delay micro-instabilities in the fibre direction, allowing the longitudinal yarns to carry higher loads.

It is noted that the variation in the test results of laminate *DTO240* is atypically high (Table 6). However, this can be attributed to the less uniform reinforcement configuration of laminate *DTO240*. In fact, a similar effect of the reduced uniformity of the microstructure was also observed by Amacher et al. [19], with thicker UD tapes showing not only lower strength but also higher variability in the test results of smooth coupons subjected to compressive failure.

5.2.3. Laminate tensile centre-notched strength test results

All CNT coupons of laminates *DTO240* and *DTO160* exhibited an approximately linear response, with small load drops observed close to the peak load, with no effect on the stiffness of the specimens. These small load drops can be attributed to internal damage growth from the notch tips, which blunted the strain concentration and modified the surface strain fields (Fig. 12). In laminate *DTO240* (Fig. 12a) transverse split cracks formed in the 90° spread-tow yarns, while longitudinal splitting at the vicinity of the notch tips blunted the strain concentration, preventing further intralaminar damage growth until catastrophic failure of the 0° spread-tow yarns. On the other hand, in laminate *DTO160* (Fig. 12b), intralaminar damage growth from the notch tips started close to the peak remote stress and propagated quickly across the width, along the off-axis directions. Longitudinal split cracking tangent to the notch tips was also observed, however without preventing the occurrence of intralaminar damage growth from the notch tips.

Both laminates exhibited a fibre-dominated pull-out failure mode. However, laminate *DTO240* exhibited a more diffuse failure zone; some specimens did not exhibit a clear fracture plane, whereas others exhibited diffuse fracture predominantly along the $-45°$ direction, including pull-out and delamination

of large fibre bundles. Laminate *DTO160* exhibited fracture predominantly along the $-45°$ direction, with fibre bundle pull-out and delaminations with a triangular shape due to intralaminar fracture along the $45°$ direction of some off-axis STF layers. Longitudinal splitting of the $0°$ spread-tow yarns was observed in the specimens of both laminates.

Table 7 shows the average results for the ultimate remote stress of the CNT tests. It is interesting to note that the tensile centre-notched strengths of laminates *DTO240* and *DTO160* differ by just 0.9%, in spite of the differences in the morphology and extent of the failure mechanisms involved in the fracture process. The similarity of the experimental results can be attributed to the development of internal longitudinal split cracking tangent to the notch tips before ultimate failure of both laminates (Fig. 12). However, the susceptibility of the thicker spread-tow yarns of laminate *DTO240* to develop early subcritical damage results in a diffuse failure mode due to the propagation of transverse and longitudinal split cracking.

5.2.4. Laminate compressive centre-notched strength test results

Centre-notched coupons of laminates *DTO240* and *DTO160* were also tested to failure in compression. Interestingly, before ultimate failure, the morphology and extent of damage was very similar in both laminates. Damage propagation from the notch tips started early before ultimate failure, but substantial damage growth did not occur until that point, remaining confined to the vicinity of the notch tips.

Small load drops were observed in some specimens of laminate *DTO240*, close to or after the peak load. These load drops, which had a negligible effect on the stiffness of the tested specimens, were attributed to the development of the damage process zone ahead of the notch tips. In laminate *DTO160*, no load drops were observed, suggesting that the development of the damage process zone had a much lower effect on the response of laminate *DTO160* than in laminate *DTO240*.

Unstable propagation across the ligament width occurred just upon ultimate

failure. Both laminates exhibited a catastrophic failure mode, characterised by a steep load drop. All specimens exhibited a net-section failure mode (Fig. 13). However, failure of laminate *DTO240* was characterised by a complex combination of damage mechanisms, including fibre kinking, wedge transverse fracture and surface fibre/matrix splitting caused by buckling of the outer STF layers (Fig. 13a). On the other hand, failure of laminate *DTO160* was characterised predominantly by fibre kinking, which propagated across the ligament section ahead of the notch tips (Fig. 13b). Clear kink bands formed through the thickness of the laminate, along a plane inclined with respect to the loading direction. Small longitudinal split cracks at the lateral free edges were also observed is some specimens, due to buckling of the thin outer layers.

Table 7 shows the mean values of the ultimate remote stress of the CNC tests and corresponding coefficients of variation (C.V.). Following the trends observed for the compressive unnotched strength (Sect. 5.2.2), laminate *DTO160* is characterised by an improved compressive notched response, with a compressive centre-notched strength 10.3% higher than laminate *DTO240*. The more brittle failure mode of laminate *DTO160*, attributed to a better uniformity of the thin 160 g/m^2 spread-tow yarns that delays the onset of the micro-instabilities that lead to compressive failure, results in an improved compressive response either or not in the presence of stress concentrations, which can be relevant for a number of industrial applications, including in aerospace.

5.2.5. OHT test results

All OHT specimens exhibited an approximately linear response until ultimate failure. Small load drops were observed close to the peak load (clearer in the large OHT specimens, with a hole diameter of 5 mm), caused by damage growth at the vicinity of the open hole just before unstable catastrophic failure.

The small OHT specimens of both laminates exhibited longitudinal split cracking tangent to the hole boundary, resulting in an important blunting effect that precluded stable intralaminar cracking across the ligament section before catastrophic failure of the longitudinal spread-tow yarns (Fig. 14). In the large

OHT specimens (Fig. 15), intralaminar cracking perpendicular to the loading direction was observed in both laminates, which started propagating early before ultimate failure. After stable propagation, transverse intralaminar fracture eventually originated other damage mechanisms ahead of the crack tips, in particular longitudinal splitting. It was also noted that, in general, internal damage growth was delayed in laminate *DTO160*.

Both laminates exhibited a fibre-dominated pull-out failure mode, independently of the coupon geometry. Laminate *DTO240* exhibited a diffuse fracture plane either perpendicular or at 45° with the loading direction, dominated by fibre bundle pull-out and split cracking of the longitudinal and off-axis spread-tow yarns. Transverse split cracking and delamination of the outer STF layers were also observed. Laminate *DTO160* exhibited a more brittle failure mode, with the fracture plane predominantly at 45° with the loading direction. Fibre bundle pull-out and split cracking of the longitudinal and off-axis spread-tow yarns were also observed, but in lesser extent than in laminate *DTO240*. Laminate *DTO160* also exhibited delaminations with triangular shape across the ligament section. The damage morphology of each laminate was similar in both coupon geometries, even though the extent of diffuse damage increased with specimen size in both cases.

Table 7 shows the average results for the ultimate remote stress of the OHT tests, and corresponding coefficients of variation. Interestingly, for the specimens with a hole diameter of 2 mm, laminate *DTO160* exhibits an ultimate remote stress 4.9% higher than laminate *DTO240*. Because the ligament section is sufficiently small, the extent of diffuse damage observed in both laminates is enough to effectively blunt the notch (Fig. 14), while the stronger unnotched ligaments of laminate *DTO160* contribute for a slightly higher tensile notched strength. On the other hand, the ultimate remote stress of the specimens with a hole diameter of 5 mm is virtually the same, as it differs by just 1.4%. In this case, notch blunting in laminate *DTO160* is not so effective (Fig. 15b), leading to a notched strength reduction (in the range of 7.3%) with increasing hole diameter. In laminate *DTO240*, though, due to its higher susceptibility to develop

subcritical damage mechanisms with a significant blunting effect (Fig. 15a), the notched strength remains virtually unchanged with increasing hole diameter (for the hole diameter range studied in the present work); hence, it can be expected that, as the specimen size increases, the tensile notched strength of laminate *DTO240* will become higher than the tensile notched strength of laminate *DTO160*. Nevertheless, the difference is not remarkable, suggesting that thin STFs can be effectively used in notched structures subjected to tensile loads (see also Sect. 5.2.3), in particular if other criteria such as high unnotched strengths and/or improved compressive behaviour are also to be taken into account.

5.2.6. OHC test results

A linear response was obtained in all OHC specimens of both laminates, which exhibited a catastrophic failure mode, characterised by a steep load drop. Intralaminar compressive damage growth from the vicinity of the hole boundary started early in both laminates. Before ultimate failure, intralaminar compressive damage propagated stably but quickly across the ligament section in laminate *DTO240*, whereas in laminate *DTO160* it propagated unstably upon ultimate failure. The ability of laminate *DTO160* to delay through-the-width propagation of intralaminar damage resulted in an improved compressive notched response (Table 7).

After testing, all specimens exhibited a net-section failure mode (Fig. 16). However, failure of laminate *DTO240* was characterised by a complex combination of damage mechanisms, including fibre kinking, wedge transverse fracture and surface fibre/matrix splitting caused by buckling of the outer STF layers (Fig 16a). Failure of laminate *DTO160* was dominated by fibre kinking, which propagated across the ligament section ahead of the hole boundary (Fig. 16b). Clear kink bands formed through the thickness of the laminate, along a plane inclined with respect to the loading direction. Surface splitting due to intralaminar compressive fracture of the outer STF layers along the fracture plane was also observed.

Table 7 shows the average results for the ultimate remote stress of the OHC

tests and corresponding coefficients of variation. Following the trends of the unnotched and centre-notched compression tests (Sects. 5.2.2 and 5.2.4, respectively), laminate *DTO160* exhibits an improved compressive notched response, with an open-hole compressive strength 7.4% higher than laminate *DTO240*. Interestingly, it is noted that, whereas subcritical damage growth in notched coupons acts as a blunting mechanism in tension (Sects. 5.2.3 and 5.2.5), in compression it seems to contribute for early fracture of the longitudinal spread-tow yarns, as observed in the unnotched configuration (Sect. 5.2.2). Precluding the propagation of subcritical damage, as observed in laminate *DTO160*, can delay longitudinal compressive failure, improving the compressive response.

5.2.7. Bearing test results

Bolt-bearing tests were performed on laminates *DTO240* and *DTO160* to assess the effect of tow thickness on the performance of STF mechanically fastened joints. As expected, all specimens exhibited a bearing failure mode, resulting from local compressive damage in the bearing hole region. Besides local compressive failure and crushing of the load-bearing surface, which is the typical failure mode observed in composite laminates subjected to bearing loads [13, 22], split cracking of the longitudinal and transverse spread-tow yarns of the outer layers was also observed in the region outside the washer, after permanent deformation of the hole. No relevant difference between the failure modes of laminates *DTO240* and *DTO160* was observed.

The bearing stress-bearing strain curves [10] of both laminates were linear up to approximately 50% of the maximum bearing stress, exhibiting a small kink before the response becomes nonlinear (a similar response was already reported in previous work [13]). Micrographs taken from the bearing plane of interrupted tests showed that the nonlinearity in the bearing stress-bearing strain curves was caused by the propagation of fibre kinking and shear-driven matrix cracking, as well as fibre crushing along the inner 0° spread-tow yarns (Figs. 17a and 18a). It was also noted that the extent of matrix cracking in laminate *DTO160* was noticeably lower than in laminate *DTO240*, indicating that compressive matrix-

dominated fracture was effectively delayed in the thinner STFs due to an *in situ* effect in compression [23].

For bearing stresses greater than the initial peak bearing stress, extensive fibre kinking and shear-driven matrix cracking were observed (Figs. 17b and 18b). These damage mechanisms were not restricted to the vicinity of the hole edge, occurring along the bearing plane far from the loading surface. Moreover, their interaction led to the formation of through-the-thickness shear cracks, which were responsible for the first load drops. It is also interesting to note that laminate *DTO160* exhibited a "more brittle" longitudinal compressive failure mode, with more pronounced kink bands along the 0° spread-tow yarns, as well as shear-driven fibre fractures.

After the first load drop and formation of the first through-the-thickness shear cracks, further loading lead to additional matrix cracking and fibre kinking, promoting the formation and propagation of the shear cracks along the bearing plane. Subsequent hole deformation also caused additional fibre and matrix crushing at the hole edge.

Table 8 shows the average test results and respective coefficients of variation for the bearing strengths of laminates *DTO240* and *DTO160* adopting some of the most common bearing strength definitions used in the literature, namely the average bearing stress at the onset of nonlinearity, the average bearing stress for an offset bearing strain of 2%, the average bearing stress at the first load drop, and the average maximum bearing stress. The bearing stress and the offset bearing strain were determined following the ASTM D5961/D5961M – 13 test standard [10].

As can be observed, because the governing failure mechanisms were essentially the same, laminates *DTO240* and *DTO160* exhibit virtually the same bearing response, independently of the bearing strength definition (Table 8). The only exception is the average bearing stress for an offset bearing strain of 2%, which is 5% higher in laminate *DTO160*. This can be attributed to the ability of the thinner STF to delay the propagation of compressive subcritical damage mechanisms before severe hole deformation.

It is interesting to note that, whereas previous studies [13, 19] have shown that the structural performance of mechanically fastened joints of thin-ply laminates can be considerably better than laminates with thicker UD plies, the same thickness effect was not observed in the present study, in spite of the improved compressive response of the thinner 160 g/m^2 STF. This is perhaps due to the less significant difference between the thickness of the yarns when compared with previous studies [13, 19], and also due to the fact that the yarns of both STFs were obtained by tow spreading, ensuring a good homogeneity of the microstructure in spite of the different tow thicknesses. Nevertheless, it can be expected that, for a wider range of tow thicknesses, or for a comparison with conventional textile composites with less uniform meso-structures, the damage suppression capability of the thin yarns will play a positive role in improving the bearing response of advanced textile composites.

6. Conclusions

With the aim to study the structural response of aerospace-grade plain weave STFs of different tow thicknesses, an experimental test campaign was carried out which included basic characterisation of the STFs and the detailed assessment of the structural response of laminates based on a baseline of the aeronautical industry.

Characterisation tests showed that the thin STF exhibited lower tensile strength than the thick STF, attributed to the superior ability of the latter to develop subcritical damage growth that apparently resulted in a stress relaxation of the longitudinal yarns, consequently delaying ultimate failure. In compression, though, the trend changes dramatically. The thin STF exhibited a compressive unnotched strength 16.2% higher than the thick STF, in agreement with what has been observed in UD tapes [19]. This improved behaviour can be attributed to the uniformity of the thin spread-tow yarns, including lower fibre waviness and smaller crimp angles, which delays micro-instabilities in the fibre direction and, consequently, improves the longitudinal strength. Off-axis compression

tests also showed that, when subjected to combined compression/in-plane shear loads, the thin STF is characterised by an improved overall compressive resistance. Using the obtained off-axis data, it was possible to estimate the in-plane shear strengths of the STFs, showing that the thin STF also exhibits an improved in-plane shear response over the thick STF, attributed to an *in situ* effect in shear [20].

At the laminate level, as expected, the thin-STF laminate exhibited a tensile unnotched strength 13.9% higher than the thick-STF laminate. This improved unnotched response, already observed in multidirectional tape laminates [13, 17–19], was attributed to the damage suppression capability of laminates made of thinner reinforcements. By precluding subcritical damage mechanisms, the thin-STF laminate was able to sustain reasonably higher applied loads. It is noted that the apparent superior longitudinal strength of the thick STF did not translate into a superior laminate strength. In compression, following the trend of the UD STF laminates, an improvement of the compressive unnotched strength of 17.7% was observed for the thin-STF laminate when compared with the thick-STF laminate.

Interestingly, the tensile notched strengths of the multidirectional STF laminates did not differ substantially, in spite of some differences in the morphology and extent of the failure mechanisms involved in the fracture process. The similarity of the notched responses can be attributed to the development of internal longitudinal split cracking tangent to the notch tips before ultimate failure of both laminates. In compression, following the trends observed for the smooth coupons, the thin-STF laminate exhibited an improved compressive notched response. Finally, a similar bearing response was obtained for both STF laminates. The thin-STF laminate exhibited a slightly higher resistance to the propagation of subcritical damage mechanisms at the initial stages of permanent damage, but the resistance to severe damage growth was virtually the same.

Acknowledgements

This work was funded by AIRBUS under project 2genComp — second generation Composites. The authors gratefully acknowledge the support provided by AIRBUS.

The authors are also grateful to Oxeon AB (Borås, Sweden) for providing the spread-tow fabrics used in the experimental test campaign reported in this paper.

The first author would like to thank the financial support provided by FCT – Fundação para a Ciência e a Tecnologia through National Funds in the scope of project MITP-TB/PFM/0005/2013.

The last author gratefully acknowledges the funding of Project NORTE-01-0145-FEDER-000022 – SciTech – Science and Technology for Competitive and Sustainable Industries, co-financed by Programa Operacional Regional do Norte (NORTE2020), Fundo Europeu de Desenvolvimento Regional (FEDER).

References

[1] El-Dessouky HM, Lawrence CA, McGrail T, Broughton WR. Ultra-lightweight carbon fibre/thermoplastic composite material using spread tow technology. Compos Part B-Eng 2013;50:91–7.

[2] Shamsudin MH, York CB. Mechanically coupled laminates with balanced plain weave. Compos Struct 2014;107:416–28.

[3] Nishikawa Y, Okubo K, Fujii T, Kawabe K. Fatigue crack constraint in plain-woven CFRP using newly-developed spread tows. Int J Fatigue 2006;28:1248–53.

[4] Jacques S, De Baere I, Van Paepegem W. Application of periodic boundary conditions on multiple part finite element meshes for the meso-scale homogenization of textile fabric composites. Compos Sci Technol 2014;92:41–54.

[5] Standard test method for tensile properties of polymer matrix composite materials, ASTM D3039/D3039M – 14. ASTM International; West Conshohocken, PA, USA; 2014.

[6] Koerber H, Xavier J, Camanho PP, Essa YE, Martín de la Escalera F. High strain rate behaviour of 5-harness-satin weave fabric carbon-epoxy composite under compression and combined compression-shear loading. Int J Solids Struct 2015;54:172–82.

[7] Bing Q, Sun CT. Specimen size effect in off-axis compression tests of fiber composites. Compos Part B-Eng 2008;39:20–6.

[8] Standard test method for open-hole compressive strength of polymer matrix composite laminates, ASTM D6484/D6484M – 14. ASTM International; West Conshohocken, PA, USA; 2014.

[9] Standard test method for open-hole tensile strength of polymer matrix composite laminates, ASTM D5766/D5766M – 11. ASTM International; West Conshohocken, PA, USA; 2011.

[10] Standard test method for bearing response of polymer matrix composite laminates, ASTM D5961/D5961M – 13. ASTM International; West Conshohocken, PA, USA; 2013.

[11] Laurin F, Charrier JS, Lévêque D, Maire JF, Mavel A, Nuñez P. Determination of the properties of composite materials thanks to digital image correlation measurements. Procedia IUTAM 2012;4:106–15.

[12] Erçin GH, Camanho PP, Xavier J, Catalanotti G, Mahdi S, Linde P. Size effects on the tensile and compressive failure of notched composite laminates. Compos Struct 2013;96:736–44.

[13] Arteiro A, Catalanotti G, Xavier J, Camanho PP. Notched response of non-crimp fabric thin-ply laminates. Compos Sci Technol 2013;79:97–114.

687 [14] Caminero MA, Lopez-Pedrosa M, Pinna C, Soutis C. Damage monitor-
688 ing and analysis of composite laminates with an open hole and adhe-
689 sively bonded repairs using digital image correlation. Compos Part B-Eng
690 2013;53:76–91.

691 [15] Arteiro A, Catalanotti G, Xavier J, Camanho PP. Large damage ca-
692 pability of non-crimp fabric thin-ply laminates. Compos Part A-Appl S
693 2014;63:110–22.

694 [16] GOM International AG. Bremgarterstrasse 89B, CH-8967 Widen, Switzer-
695 land; 2000.

696 [17] Sihn S, Kim RY, Kawabe K, Tsai SW. Experimental studies of thin-ply
697 laminated composites. Compos Sci Technol 2007;67:996–1008.

698 [18] Wisnom MR, Khan B, Hallett SR. Size effects in unnotched tensile strength
699 of unidirectional and quasi-isotropic carbon/epoxy composites. Compos
700 Struct 2008;84:21–8.

701 [19] Amacher R, Cugnoni J, Botsis J, Sorensen L, Smith W, Dransfeld C. Thin
702 ply composites: Experimental characterization and modeling of size-effects.
703 Compos Sci Technol 2014;101:121–32.

704 [20] Camanho PP, Dávila CG, Pinho ST, Iannucci L, Robinson P. Prediction
705 of in situ strengths and matrix cracking in composites under transverse
706 tension and in-plane shear. Compos Part A-Appl S 2006;37:165–76.

707 [21] Tsai SW, Melo JDD. Composite Materials Design and Testing — Unlocking
708 mystery with invariants. Stanford: Composites Design Group, Department
709 of Aeronautics and Astronautics, Stanford University; 2015.

710 [22] Camanho PP, Lambert M. A design methodology for mechanically fastened
711 joints in laminated composite materials. Compos Sci Technol 2006;66:3004–
712 20.

[23] Arteiro A, Catalanotti G, Melro AR, Linde P, Camanho PP. Micro-mechanical analysis of the effect of ply thickness on the transverse compressive strength of polymer composites. Compos Part A-Appl S 2015;79:127–37.

[24] Xavier J, de Jesus AMP, Morais JJL, Pinto JMT. Stereovision measurements on evaluating the modulus of elasticity of wood by compression tests parallel to the grain. Constr Build Mater 2012;26(1):207–15.

[25] Catalanotti G, Xavier J, Camanho PP. Measurement of the compressive crack resistance curve of composites using the size effect law. Compos Part A-Appl S 2014;56:300–7.

List of Figures

1 Virtual strain gauges and remote stress-strain relations of representative UD plain weave unnotched tension test specimens obtained with the DIC technique. The loading direction is parallel to the horizontal axis of the specimens. 30

2 (Top) Coloured distributions of grey levels (0–255), (middle) longitudinal strain fields, ε_x, and (bottom) local longitudinal strain along the edges of the outer STF layer (red and black dashed lines) of representative UD unnotched tension test specimens of laminates (i) *UDA240* and (ii) *UDA160* obtained with the DIC technique at the stage prior to ultimate failure. The reference DIC coordinate system is shown in the top figures, where the x-axis is aligned with the loading direction. 31

3 Representative UD plain weave unnotched tension test specimens after testing. 32

4 Representative UD plain weave unnotched compression test specimens after testing. 32

5 Representative 15° off-axis compression test specimens after testing. 33

6 Representative 30° off-axis compression test specimens after testing. 33

7 Failure envelopes for the combined compression/in-plane shear stress space. 34

8 Virtual strain gauges and remote stress-strain relations of representative unnotched tension test specimens obtained with the DIC technique. The loading direction is parallel to the horizontal axis of the specimens. 34

9 (Top) Coloured distributions of grey levels (0–255), (middle) longitudinal strain fields, ε_x, and (bottom) local longitudinal strain along the edges of the outer STF layer (red and black dashed lines) of representative unnotched tension test specimens of laminates (i) *DTO240* and (ii) *DTO160* obtained with the DIC technique at the stage prior to ultimate failure. The reference DIC coordinate system is shown in the top figures, where the x-axis is aligned with the loading direction. 35

10 Representative unnotched tension test specimens after testing. . 35

11 Details of the laminate unnotched compression test specimens after testing. 36

12 Specimen surface and longitudinal strain fields, ε_y, of representative CNT test specimens of laminates *DTO240* and *DTO160* obtained with the DIC system before ultimate failure. The reference DIC coordinate systems are shown in the figures, where the y-axis is aligned with the loading direction. 36

13 Details of representative CNC test specimens after testing. 37

14 Specimen surface and longitudinal strain fields, ε_y, of representative OHT test specimens of laminates *DTO240* and *DTO160* with a hole diameter of 2 mm obtained with the DIC system before ultimate failure. The reference DIC coordinate systems are shown in the figures, where the y-axis is aligned with the loading direction. 37
15 Specimen surface and longitudinal strain fields, ε_y, of representative OHT test specimens of laminates *DTO240* and *DTO160* with a hole diameter of 5 mm obtained with the DIC system before ultimate failure. The reference DIC coordinate systems are shown in the figures, where the y-axis is aligned with the loading direction. 38
16 Details of the OHC test specimens after testing. 38
17 Micrographs of the bearing plane of representative bolt-bearing specimens of laminate *DTO240* after interrupted testing. Magnification factor of 5×. 39
18 Micrographs of the bearing plane of representative bolt-bearing specimens of laminate *DTO160* after interrupted testing. Magnification factor of 5×. 40

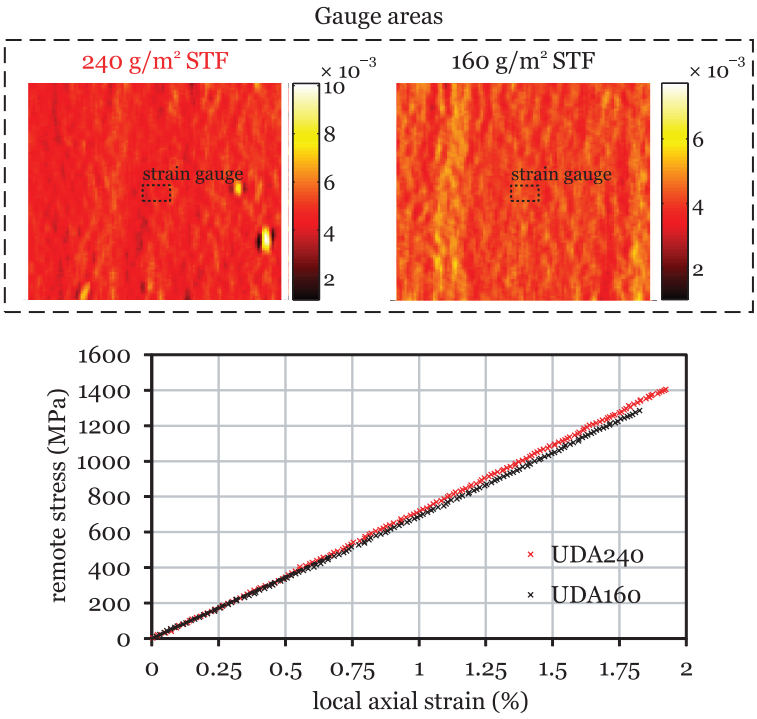

Figure 1: Virtual strain gauges and remote stress-strain relations of representative UD plain weave unnotched tension test specimens obtained with the DIC technique. The loading direction is parallel to the horizontal axis of the specimens.

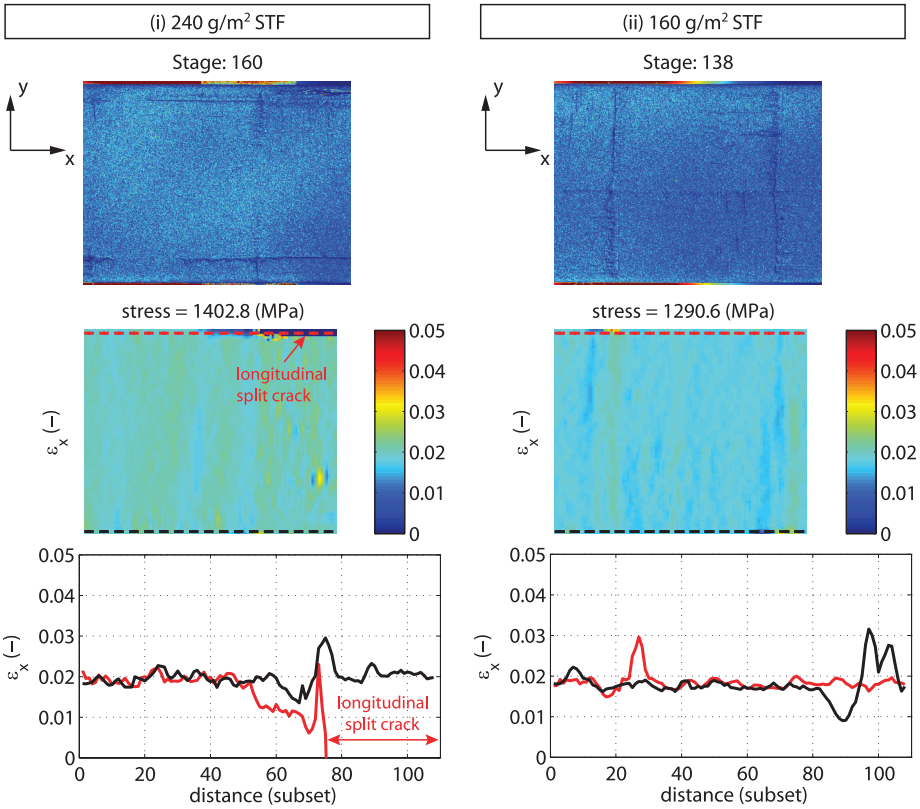

Figure 2: (Top) Coloured distributions of grey levels (0–255), (middle) longitudinal strain fields, ε_x, and (bottom) local longitudinal strain along the edges of the outer STF layer (red and black dashed lines) of representative UD unnotched tension test specimens of laminates (i) *UDA240* and (ii) *UDA160* obtained with the DIC technique at the stage prior to ultimate failure. The reference DIC coordinate system is shown in the top figures, where the x-axis is aligned with the loading direction.

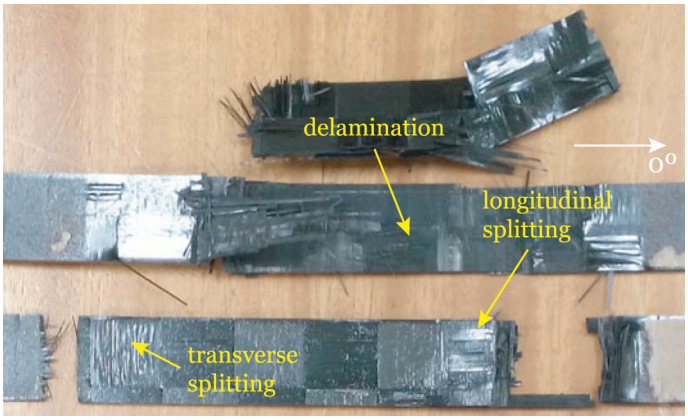

(a) Thick STF *UDA240*.

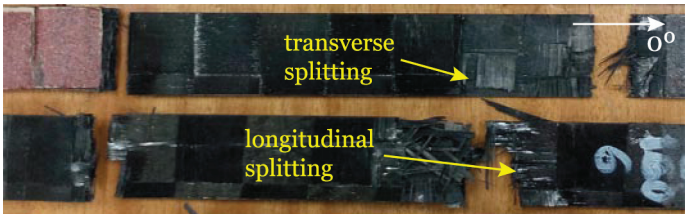

(b) Thin STF *UDA160*.

Figure 3: Representative UD plain weave unnotched tension test specimens after testing.

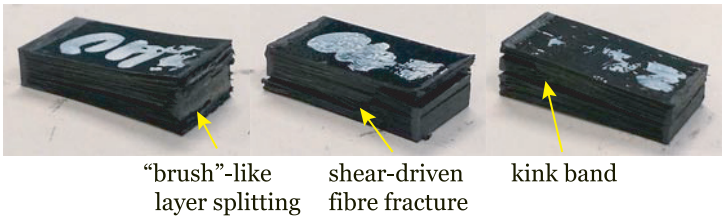

(a) Thick STF *UDB240*.

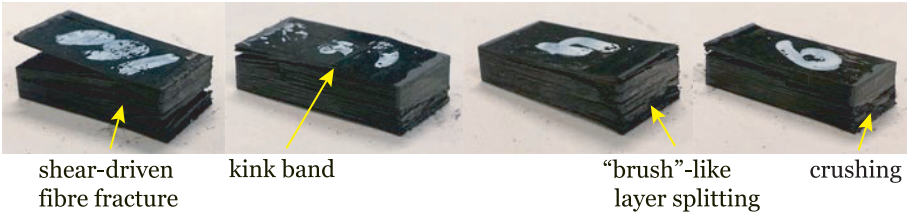

(b) Thin STF *UDB160*.

Figure 4: Representative UD plain weave unnotched compression test specimens after testing.

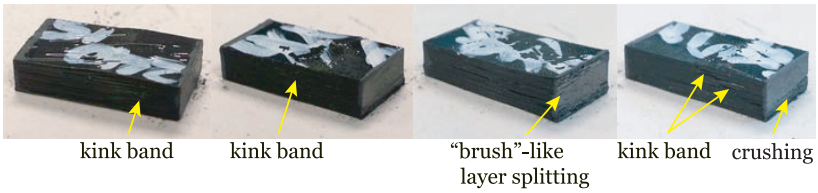

(a) Thick STF *UDB240*.

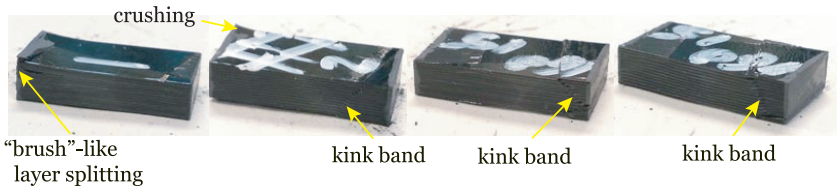

(b) Thin STF *UDB160*.

Figure 5: Representative 15° off-axis compression test specimens after testing.

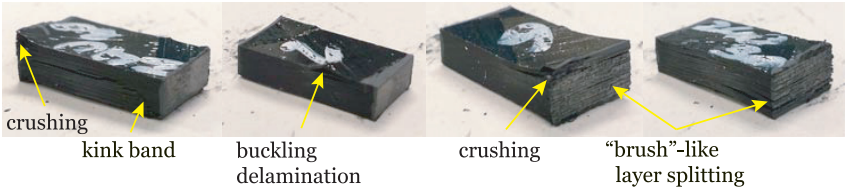

(a) Thick STF *UDB240*.

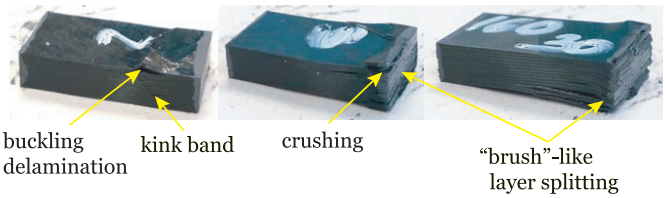

(b) Thin STF *UDB160*.

Figure 6: Representative 30° off-axis compression test specimens after testing.

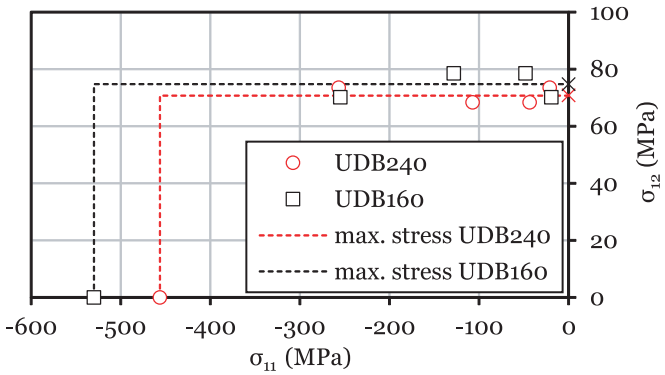

Figure 7: Failure envelopes for the combined compression/in-plane shear stress space.

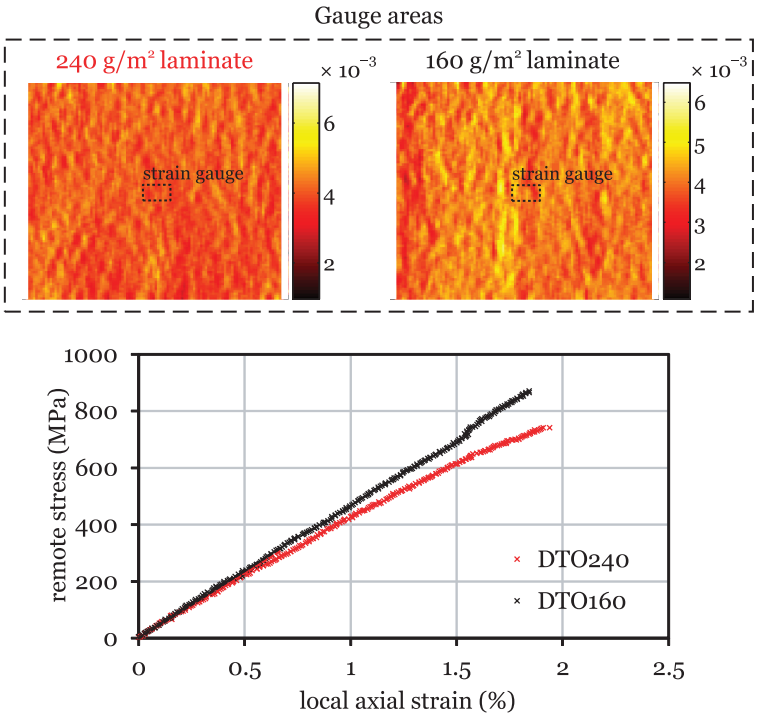

Figure 8: Virtual strain gauges and remote stress-strain relations of representative unnotched tension test specimens obtained with the DIC technique. The loading direction is parallel to the horizontal axis of the specimens.

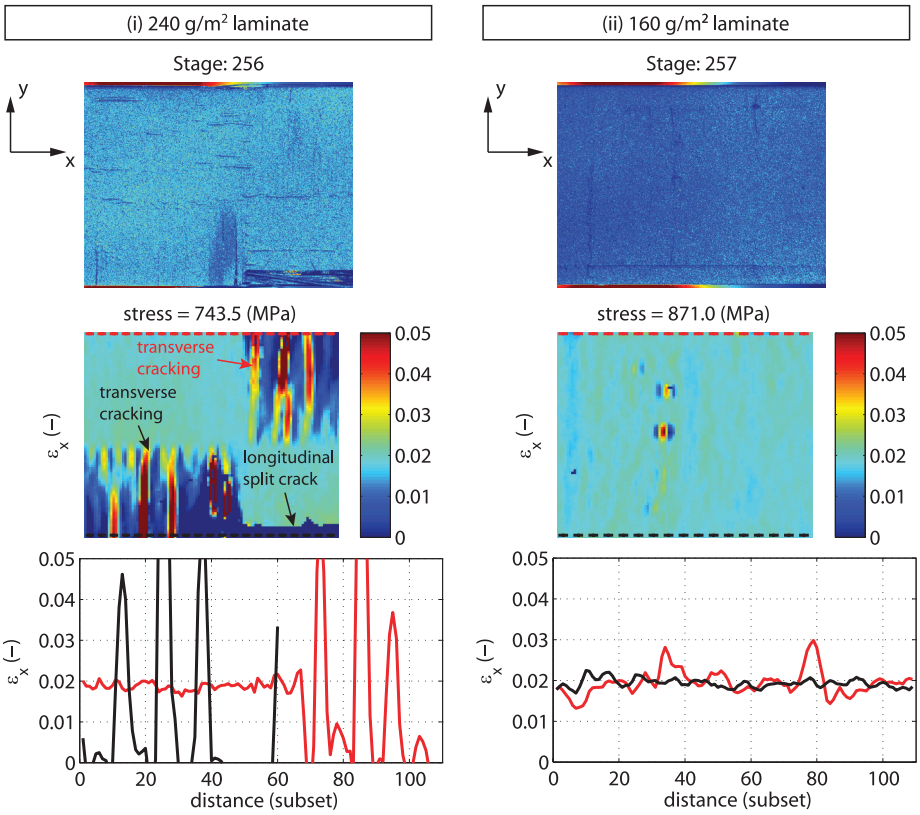

Figure 9: (Top) Coloured distributions of grey levels (0–255), (middle) longitudinal strain fields, ε_x, and (bottom) local longitudinal strain along the edges of the outer STF layer (red and black dashed lines) of representative unnotched tension test specimens of laminates (i) *DTO240* and (ii) *DTO160* obtained with the DIC technique at the stage prior to ultimate failure. The reference DIC coordinate system is shown in the top figures, where the x-axis is aligned with the loading direction.

(a) Thick-STF laminate *DTO240*.

(b) Thin-STF laminate *DTO160*.

Figure 10: Representative unnotched tension test specimens after testing.

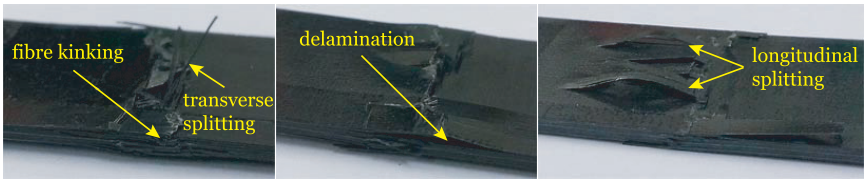

(a) Thick-STF laminate *DTO240*.

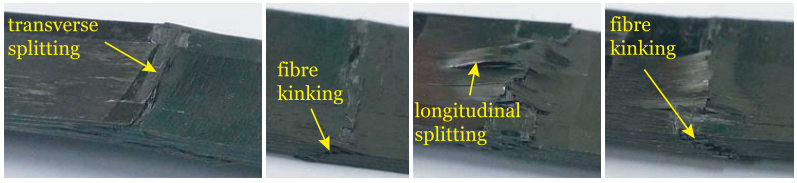

(b) Thin-STF laminate *DTO160*.

Figure 11: Details of the laminate unnotched compression test specimens after testing.

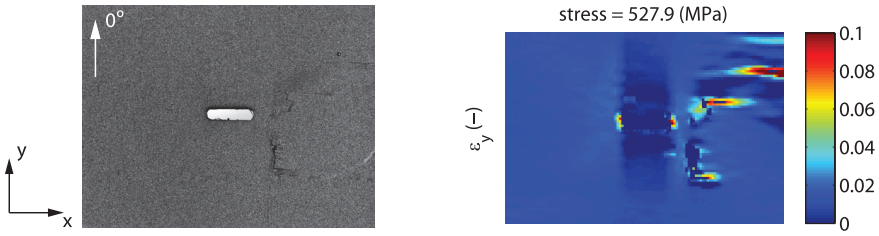

(a) Thick-STF laminate *DTO240*.

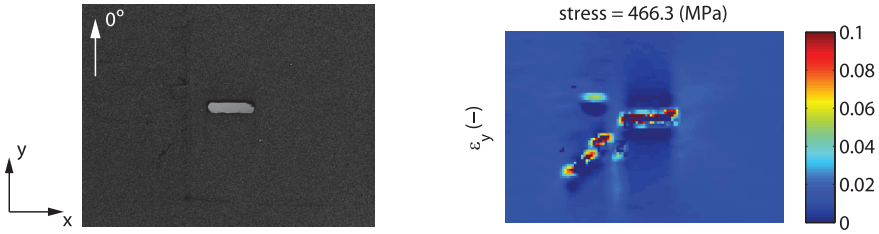

(b) Thin-STF laminate *DTO160*.

Figure 12: Specimen surface and longitudinal strain fields, ε_y, of representative CNT test specimens of laminates *DTO240* and *DTO160* obtained with the DIC system before ultimate failure. The reference DIC coordinate systems are shown in the figures, where the y-axis is aligned with the loading direction.

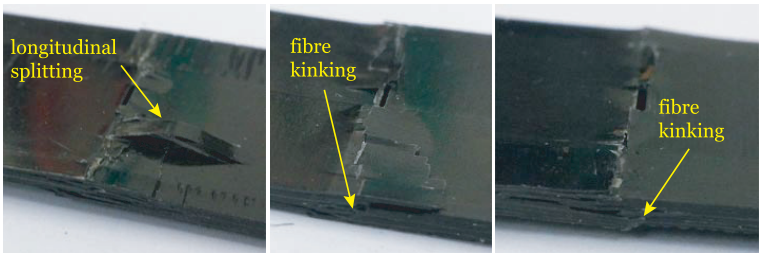

(a) Thick-STF laminate *DTO240*.

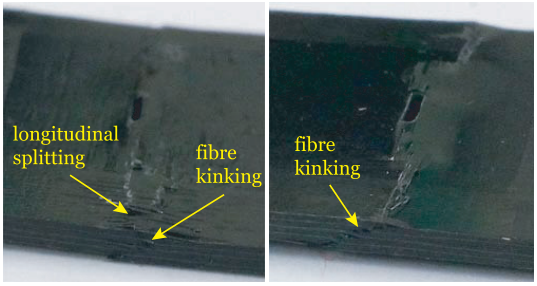

(b) Thin-STF laminate *DTO160*.

Figure 13: Details of representative CNC test specimens after testing.

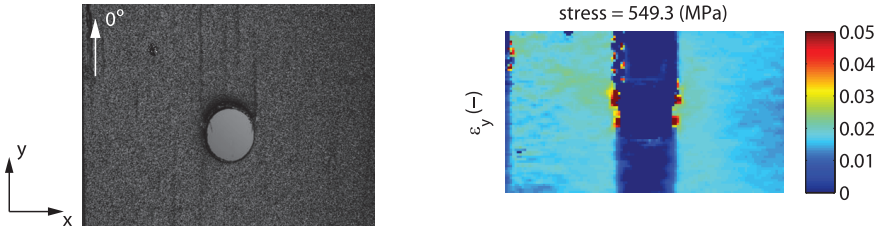

(a) Thick-STF laminate *DTO240*.

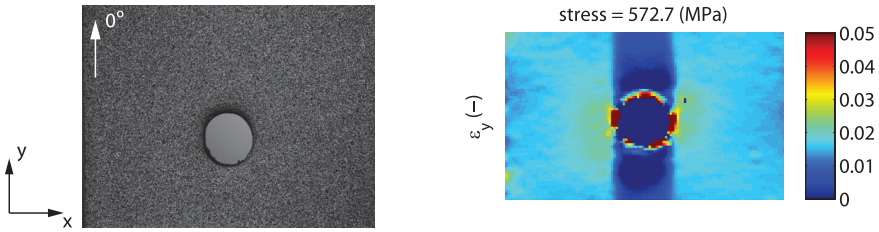

(b) Thin-STF laminate *DTO160*.

Figure 14: Specimen surface and longitudinal strain fields, ε_y, of representative OHT test specimens of laminates *DTO240* and *DTO160* with a hole diameter of 2 mm obtained with the DIC system before ultimate failure. The reference DIC coordinate systems are shown in the figures, where the y-axis is aligned with the loading direction.

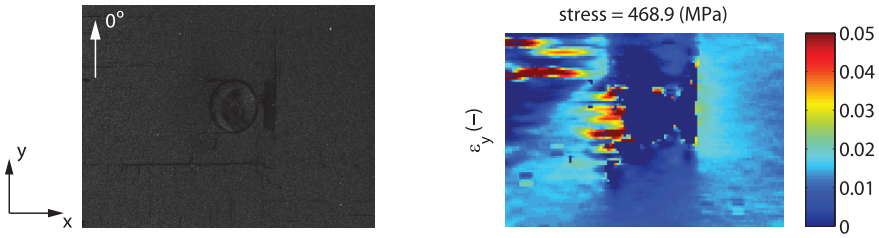

(a) Thick-STF laminate *DTO240*.

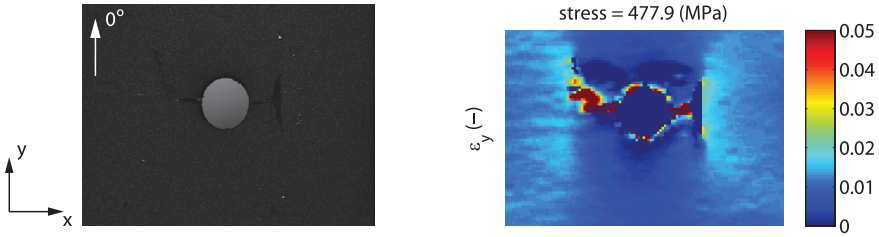

(b) Thin-STF laminate *DTO160*.

Figure 15: Specimen surface and longitudinal strain fields, ε_y, of representative OHT test specimens of laminates *DTO240* and *DTO160* with a hole diameter of 5 mm obtained with the DIC system before ultimate failure. The reference DIC coordinate systems are shown in the figures, where the y-axis is aligned with the loading direction.

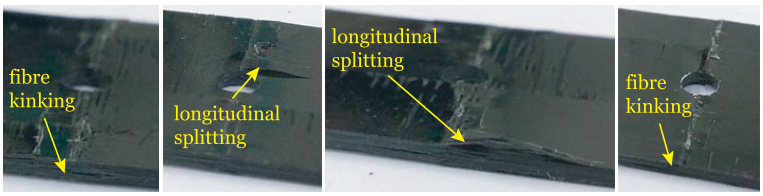

(a) Thick-STF laminate *DTO240*.

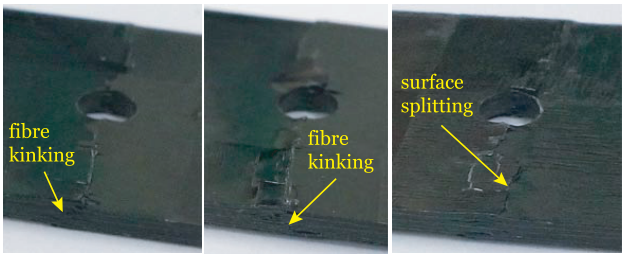

(b) Thin-STF laminate *DTO160*.

Figure 16: Details of the OHC test specimens after testing.

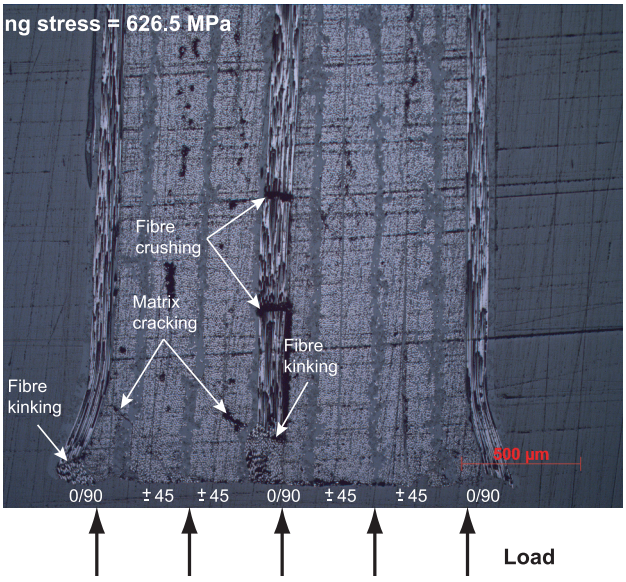

(a) Onset of nonlinearity.

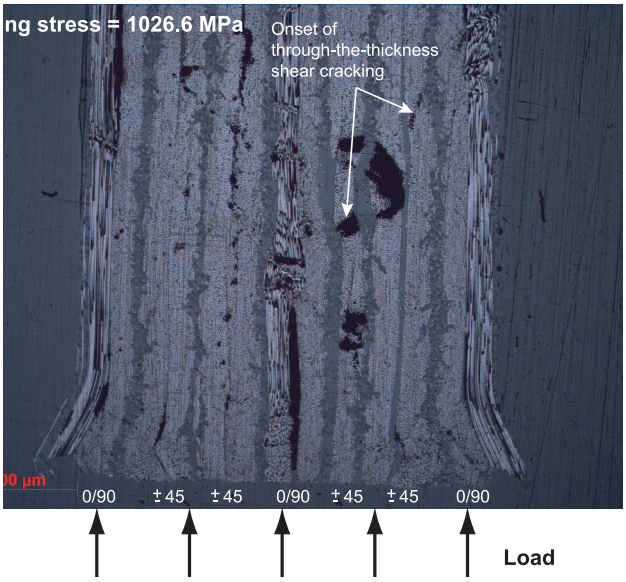

(b) First load drop.

Figure 17: Micrographs of the bearing plane of representative bolt-bearing specimens of laminate *DTO240* after interrupted testing. Magnification factor of 5×.

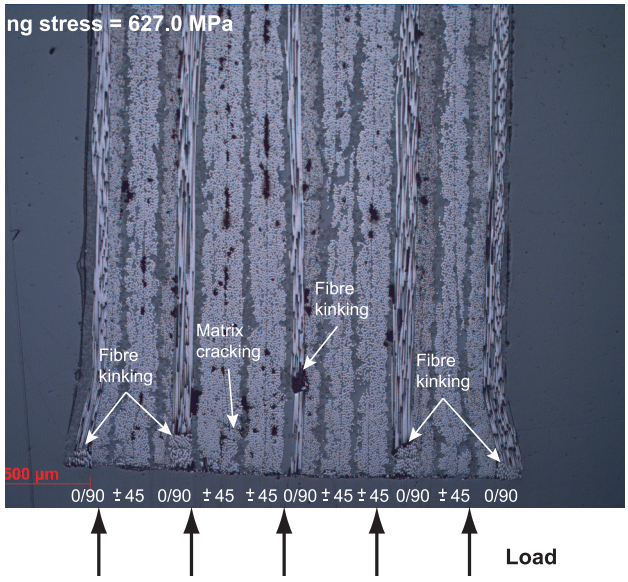

(a) Onset of nonlinearity.

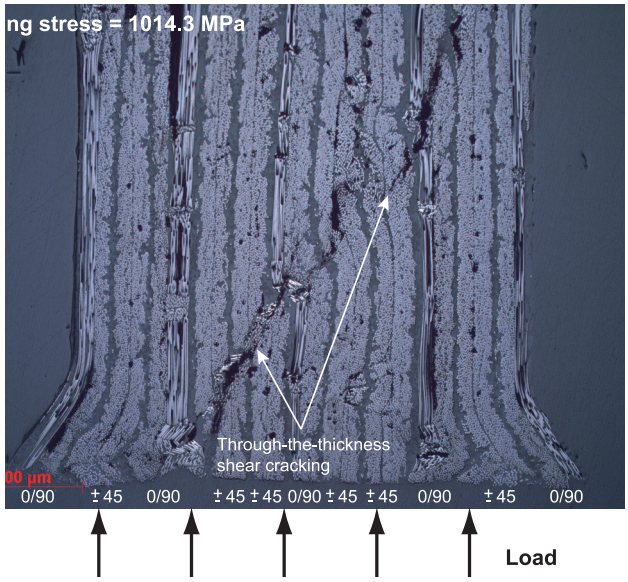

(b) First load drop.

Figure 18: Micrographs of the bearing plane of representative bolt-bearing specimens of laminate *DTO160* after interrupted testing. Magnification factor of 5×.

List of Tables

1 Stacking sequence definitions of the T700SC/M21 STF laminates. 42
2 OHT test matrix. 42
3 Configuration of the DIC system. 42
4 Unnotched tension and compression test results. 43
5 Off-axis compression test results. 43
6 Laminate tensile and compressive unnotched test results. 43
7 Laminate tensile and compressive notched test results. 43
8 Bearing test results. 44

Table 1: Stacking sequence definitions of the T700SC/M21 STF laminates.

Laminate ID	STF grade	STF stacking sequence	Nominal laminate thickness (mm)
Textile characterisation			
UDA240	240 g/m^2	$[0]_8$	1.92
UDB240	240 g/m^2	$[0]_{18}$	4.32
UDA160	160 g/m^2	$[0]_{12}$	1.92
UDB160	160 g/m^2	$[0]_{26}$	4.16
Structural characterisation			
DTO240	240 g/m^2	$[0/45_2/0/45_2/0]$	1.68
DTO160	160 g/m^2	$[0/45/0/45_2/0/45_2/0/45/0]$	1.76

Table 2: OHT test matrix.

Geometry	L_s (mm)	L (mm)	W (mm)	d (mm)
Large	300	150	30	5
Small	300	200	12	2

Table 3: Configuration of the DIC system.

Camera-lens optical system	
CCD camera	Baumer 138 Optronic FWX20 8-bit Resolution: 1624×1236 pixels^2 Sensor format: 1/1.8”
Lens	Nikon AF Micro-Nikkor 200 mm f/4D IF-ED
DIC measuring parameters	
Subset size	15×15 pixels^2
Subset step	13×13 pixels^2
Strain base length	5 subsets
Strain validity code	55.0%
Strain computation method	Total
DIC resolution	
Spatial resolution	2×10^{-2} pixels [24, 25]
Strain resolution	0.01-0.04% [24, 25]

Table 4: Unnotched tension and compression test results.

Results		240 g/m^2 STF	160 g/m^2 STF
Tension			
E_{1T}	(MPa)	66909	66229
ν_{12}	(-)	0.097	0.061
X_T	(MPa)	1408 (4.4%)†	1307 (2.8%)†
Compression			
E_{1C}	(MPa)	65089	63210
X_C	(MPa)	456 (7.5%)†	530 (3.1%)†

† Coefficients of variation (C.V.).

Table 5: Off-axis compression test results.

Results		240 g/m^2 STF	160 g/m^2 STF
15° off-axis compression			
$\bar{\sigma}_x$	(MPa)	278 (5.3%)†	274 (6.4%)†
30° off-axis compression			
G_{12}	(MPa)	8725	8317
$\bar{\sigma}_x$	(MPa)	151 (1.7%)†	176 (2.0%)†

† Coefficients of variation (C.V.).

Table 6: Laminate tensile and compressive unnotched test results.

Results		*DTO240*	*DTO160*
Tension			
E_x	(MPa)	40732	49317
$\bar{\epsilon}_x$	(%)	1.94	1.84
X_T^L	(MPa)	753 (1.3%)†	857 (2.9%)†
Compression			
X_C^L	(MPa)	381 (12.1%)†	448 (5.4%)†

† Coefficients of variation (C.V.).

Table 7: Laminate tensile and compressive notched test results.

Results	Centre notch $2a = 5$ mm		Open hole $d = 2$ mm		Open hole $d = 5$ mm	
	DTO240	*DTO160*	*DTO240*	*DTO160*	*DTO240*	*DTO160*
Tension						
$\bar{\sigma}^\infty$ (MPa)	490	494	523	548	515	508
(C.V.)	(6.2%)	(3.9%)	(6.3%)	(4.9%)	(4.9%)	(3.4%)
Compression						
$\bar{\sigma}^\infty$ (MPa)	256	283	-	-	239	257
(C.V.)	(9.9%)	(2.1%)	-	-	(0.9%)	(0.2%)

Table 8: Bearing test results.

Results	*DTO240*	*DTO160*
Average bearing stress at the onset of nonlinearity		
$\sigma^{br}_{\text{nonlin}}$ (MPa)	628	629
(C.V.)	(5.0%)	(2.7%)
Average bearing stress for an offset bearing strain of 2%		
$\sigma^{br}_{\text{2\%offset}}$ (MPa)	884	925
(C.V.)	(1.3%)	(1.6%)
Average bearing stress at the first load drop		
$\sigma^{br}_{\text{drop}}$ (MPa)	1106	1093
(C.V.)	(9.5%)	(2.8%)
Average maximum bearing stress		
σ^{br}_{max} (MPa)	1171	1184
(C.V.)	(1.9%)	(3.9%)